nanomaterials

MDPI

Article

Effect of *n*- and *p*-Doping on Vacancy Formation in Cationic and Anionic Sublattices of (In,Al)As/AlAs and Al(Sb,As)/AlAs Heterostructures

Timur S. Shamirzaev [1,2] and Victor V. Atuchin [3,4,5,6,7,*]

1 Laboratory of Physics and Technology of Heterostructures, Institute of Semiconductor Physics, SB RAS, Novosibirsk 630090, Russia; tim@isp.nsc.ru
2 Department of Physics, Novosibirsk State University, Novosibirsk 630090, Russia
3 Laboratory of Optical Materials and Structures, Institute of Semiconductor Physics, SB RAS, Novosibirsk 630090, Russia
4 Department of Applied Physics, Novosibirsk State University, Novosibirsk 630090, Russia
5 Research and Development Department, Kemerovo State University, Kemerovo 650000, Russia
6 Department of Industrial Machinery Design, Novosibirsk State Technical University, Novosibirsk 630073, Russia
7 R&D Center "Advanced Electronic Technologies", Tomsk State University, Tomsk 634034, Russia
* Correspondence: atuchin@isp.nsc.ru

Abstract: The vacancy generation dynamics in doped semiconductor heterostructures with quantum dots (QD) formed in the cationic and anionic sublattices of AlAs is studied. We demonstrate experimentally that the vacancy-mediated high temperature diffusion is enhanced (suppressed) in n- and p-doped heterostructures with QDs formed in the cationic sublattice, while the opposite behavior occurs in the heterostructures with QDs formed in the anionic sublattice. A model describing the doping effect on the vacancy generation dynamics is developed. The effect of nonuniform charge carrier spatial distribution arisen in heterostructures at high temperatures on the vacancy generation and diffusion is revealed.

Keywords: vacancy generation; recombination; semiconductor heterostructure; diffusion

check for updates

Citation: Shamirzaev, T.S.; Atuchin, V.V. Effect of *n*- and *p*-Doping on Vacancy Formation in Cationic and Anionic Sublattices of (In,Al)As/AlAs and Al(Sb,As)/AlAs Heterostructures. *Nanomaterials* **2023**, *13*, 2136. https://doi.org/10.3390/nano13142136

Academic Editor: Cesare Malagù

Received: 23 June 2023
Revised: 18 July 2023
Accepted: 21 July 2023
Published: 23 July 2023

Copyright: © 2023 by the authors. Licensee MDPI, Basel, Switzerland. This article is an open access article distributed under the terms and conditions of the Creative Commons Attribution (CC BY) license (https://creativecommons.org/licenses/by/4.0/).

1. Introduction

The carrier confinement obtained in semiconductor quantum wells (QWs) and quantum dots (QDs) attracts research attention due to their unique electronic and optical properties [1–13]. In heterostructures with quantum dots and quantum wells at high temperature, the vacancy formation leads to the material intermixing via a vacancy-mediated diffusion [14,15]. The intermixing permits modifying the energy structure [14–18], controls hyperfine interaction [19], adjusts exciton lifetime [17,20], and reduces strain gradients [21,22] in low dimensional structures.

Vacancies in semiconductors can be electrically charged [23–25]. Therefore, a strong effect of the charge-carrier concentration on the vacancy generation occurs [15,23,26–29]. The vacancy generation dependence on the carrier concentration was studied well in bulk crystals [23,26,27,30,31]. In contradistinction to bulk crystals with uniform charge carrier distribution, a redistribution of charged carriers between different layers occurs in heterostructures. We have shown recently that the redistribution of thermally generated equilibrium electrons in undoped heterostructures can strongly change the distribution of vacancy generation in real space and vacancy-mediated diffusion [16].

In this paper, we investigate the doping effect on the charged vacancy formation in cationic and anionic sublattices of bulk AlAs and the vacancy-stimulated diffusion in heterostructures with InAlAs/AlAs and AlSbAs/AlAs QDs. It is experimentally shown that the material intermixing degree upon the annealing at a fixed temperature in the cationic

sublattice is the lowest in a *p*-doped heterostructure, increasing in an undoped one, and becomes the highest in an *n*-doped heterostructure. For the anionic sublattice, the behavior is the opposite: the lowest intermixing degree takes place in an *n*-doped heterostructure and the highest one in a *p*-doped one. The experimental observation is explained in the framework of a theoretical model, taking into account the strong dependence of the charged vacancy formation rate on the charge carrier density in the bulk material and nonuniform spatial distribution of charged carriers within a heterostructure.

The paper has the following structure. In Section 2, the heterostructures and the experimental techniques are described. In Section 3, one can see the experimental data on the vacancy-mediated material intermixing in undoped as well as *n*- and *p*-doped heterostructures with QDs, formed in cationic (InAs) and anionic (AlSb) sublattices of AlAs as the functions of temperature and doping level. The theoretical model describing the negatively and positively charged vacancy formation dynamics in bulk AlAs, as well as AlAs-based heterostructures with QDs, and the model calculations of the vacancy distribution and vacancy-mediated intermixing are presented in Section 4.

2. Experiments

Heterostructures with InAs (AlSb) QDs in an AlAs matrix were grown by molecular beam epitaxy on semi-insulating (001)-oriented GaAs substrates in a Riber Compact system. The samples consisted of one layer of the QDs sandwiched between AlAs layers grown on top of a 400 nm thick GaAs buffer layer. The lower AlAs layer with 50-nm thickness was grown in all structures at the temperature of 620 °C. Then the growth was interrupted, and the substrate temperature was decreased down to 480 °C under the As flux during cooling. The InAs (AlSb) QDs were formed at 480 °C. The upper 80-nm thick AlAs layer was grown at the same substrate temperature as the corresponding InAs or AlSb layers. A 20-nm thick cap GaAs layer was grown on the top of the AlAs layer for protection. Further details for the epitaxial growth in the AlAs matrix are given in [32–35].

From the growth conditions and model calculations, we can conclude that the average composition for (In,Al)As/AlAs QDs is about $In_{0.75}Al_{0.25}As$ [32] and, for Al(Sb,As)/AlAs QDs, it is about $AlSb_{0.3}As_{0.7}$ [33]. The size and density of the lens-shaped QDs have been recently determined by transmission electron microscopy, yielding the average diameter (D_{av}) of 12 nm (the larger D_L is 16 nm and the smaller diameter D_S (8 nm) in half-widths of the QD size distribution) and a density of about 2×10^{10} dots per cm^2 for (In,Al)As/AlAs QDs [32], and the average diameter of 20 nm (the larger D_L is 25 nm and the smaller D_S (11 nm) in half-widths of the QD size distribution) and a density of about 5×10^{10} dots per cm^2 for Al(Sb,As)/AlAs QDs [33]. The relatively low QD density prevents the carrier redistribution between the QDs [36,37].

The QDs formed in cationic and anionic sublattices of AlAs have different energy spectra. In the case of (In,Al)As/AlAs QDs, the dispersion in dot size, shape, and composition within the ensemble leads to the formation of two configurations, shown in Figure 1a,b. The electron ground state shifts from the Γ- to the X-valley with the decreasing dot diameter, while the heavy-hole (hh) ground state remains at the Γ point. This corresponds to a change from a direct to an indirect bandgap in the momentum space, while the band alignment of type-I is preserved; that is, in both cases, an electron and a hole are spatially confined within the (In,Al)As QDs [38,39]. The Al(Sb,As)/AlAs QDs have a band alignment of type-II with the lowest conduction-band states at the X_{xy} minima of the AlAs conduction band and the heavy-hole (hh) ground state at the Γ point, which leads to the band structure scheme in Figure 1c [33].

The AlAs barriers in the studied structures were undoped or doped with donors (silicon) to about 3×10^{18} cm^{-3}, or acceptors (beryllium) to about 5×10^{18} cm^{-3}. The doping designs in the heterostructures with QDs are shown in Figure 2. The samples were annealed at different temperatures (T_A) in the range from 550 to 770 °C in a hydrogen flow for 10 minutes. To prevent the surface decomposition during the annealing, the samples were protected by a 150 nm thick SiO_2 layer. The degree of material intermixing

upon annealing was estimated from the emission blue-shift in the photoluminescence (PL) spectra of the heterostructures that occurs due to a decrease in the confining potential as a result of a change in the QD size and composition [22]. The samples were placed in a cryostat and the temperature for all experiments was fixed at T = 10 K. A semiconductor laser (3.07 eV) with an excitation power density of 25 W/cm^2 was used for the PL excitation. The emitted light was dispersed by a 0.5-m monochromator and detected by a cooled CCD.

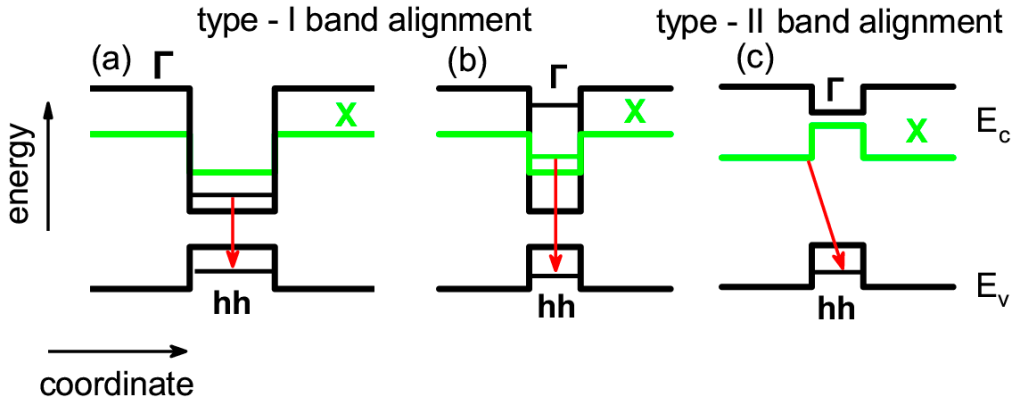


Figure 1. Schematic band diagrams of heterostructures. (**a**) Type-I direct band gap and (**b**) type-I indirect band gap, in InAlAs/AlAs QDs with large and small size; (**c**) indirect band gap with type-II in AlSbAs/AlAs QDs. Red arrows mark optical transitions of the exciton to the system ground state.

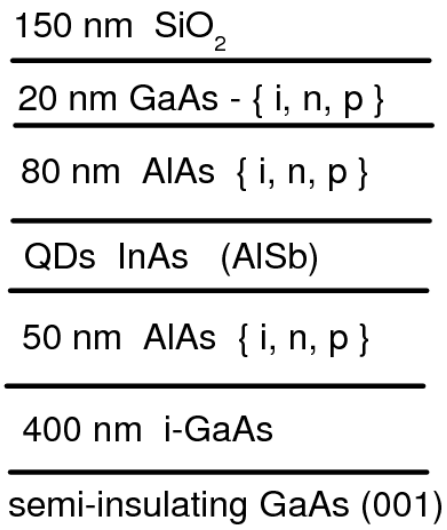


Figure 2. Scheme of the doping design in the heterostructures with QDs.

3. Experimental Results

The PL spectra of undoped heterostructures with (In,Al)As/AlAs and Al(Sb,As)/AlAs QDs annealed at different temperatures are shown in Figure 3a,d, respectively. The spectrum of the unannealed (as-grown) structure (black line) has its maximum PL_{max} = 1.72 eV (1.78 eV) for the emission in indirect bandgap QDs (In,Al)As with the band diagram shown in Figure 1b (band diagram of Al(Sb,As) QDs shown in Figure 1c.) The large emission band width is due to the dispersion of the QD parameters since the exciton energy depends on the QD size, shape, and composition [32,33]. The low energy shoulder in the spectra of (In,Al)As/AlAs QDs is a contribution of direct bandgap QDs (see Figure 1a) as it was shown in [32,40]. The spectra of the as-grown n-doped (with donor concentration 5×10^{18} cm^{-3}) and p-doped (with acceptor concentration 5×10^{18} cm^{-3}) heterostructures have a similar shape (see Figure 3). A 10 min annealing at T_A = 550 °C and below does not affect the shape of the photoluminescence spectra for all structures. With further increases

in the annealing temperature, the PL band monotonically shifts to the high-energy region of the spectrum (demonstrates the blue-shift). One can see that the annealing temperature corresponding to the onset of the PL band blue-shift and to the blue-shift magnitude at a specific temperature depends on the doping type and level. The PL band shape reflects the QDs' size distribution. Since the PL band shape is changed with annealing mainly due to a stronger shift of the low energy side of the PL band, we can conclude that interdiffusion is more pronounced in large-size QDs than that in small-size QDs.

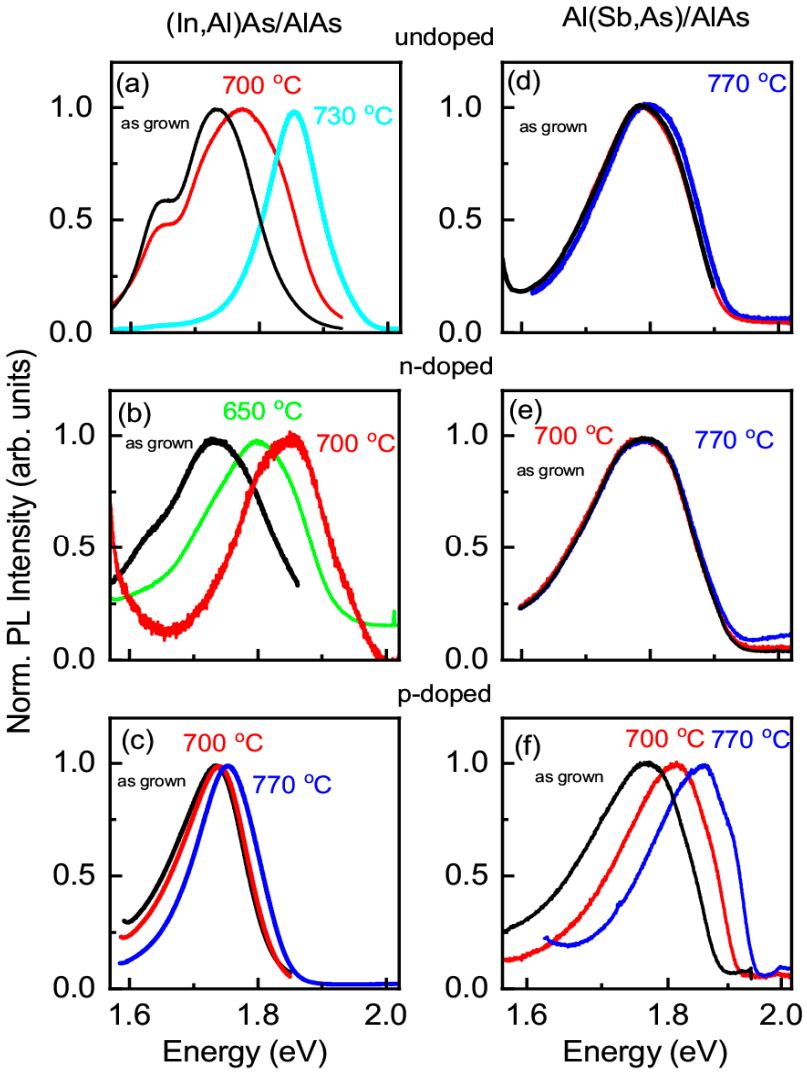


Figure 3. PL spectra measured at 10 K of (**a**–**c**) (In,Al)As/AlAs QDs and with (**d**–**f**) Al(Sb,As)/AlAs QDs annealed at different temperatures: as-grown (black), 650 °C (green), 700 °C (red), 730 °C (cyan), and 770 °C (blue); (**a**,**d**) undoped, (**b**,**e**) *n*-doped (with donor concentration 3×10^{18} cm^{-3}), (**c**,**f**) *p*-doped (with acceptor concentration 5×10^{18} cm^{-3}) heterostructures.

In the heterostructure with *n*-doped (In,Al)As/AlAs QDs, the PL band blue-shift is observed already at T_A = 600 °C, and such shift is increased strongly at higher temperatures, as it is seen in Figure 3b. For the undoped and *p*-doped heterostructures with (In,Al)As/AlAs QDs, the blue-shift takes place above T_A = 650 °C (see Figure 3a,c), and, in the *p*-doped heterostructure, this shift, at a fixed temperature in the range from 650 °C up to 770 °C, is noticeably smaller than that in the undoped one. For heterostructures with Al(Sb,As)/AlAs QDs, the blue-shift is observed already at T_A = 600 °C in the case of *p*-doping, while, in the case of *n*-doping, we do not have any blue-shift up to 770 °C (see Figure 3d,f). The shifts of the PL band maximum position relative to $h\nu_{max}$ of the as-grown

structures as a function of annealing temperature for the heterostructures with QDs formed in the cationic and anionic sublattices are collected in Figure 4a,b, respectively.

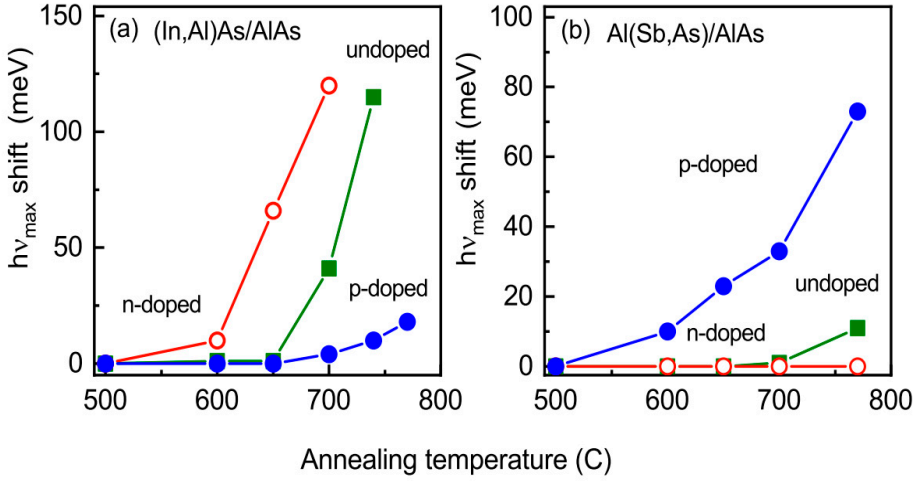


Figure 4. Shift of the PL band maximum position in the spectra with (**a**) (In,Al)As/AlAs QDs and (**b**) Al(Sb,As)/AlAs QDs with different doping types and levels depending on the annealing temperature. Undoped (olive), *n*-doped (with donor concentration 3×10^{18} cm^{-3}) (red), and *p*-doped (with acceptor concentration 5×10^{18} cm^{-3}) (blue).

Let us summarize the most important experimental findings:

(1) The intermixing of materials, that leads to a high-energy shift of the PL band due to the QD atom diffusion into the AlAs matrix during high-temperature annealing, depends strongly on the level and type of doping.
(2) For (In,Al)As quantum dots forming in the AlAs cationic sublattice, this blue-shift under the same annealing conditions is the smallest in the *p*-doped heterostructure, increases in the undoped one, and becomes the largest in the *n*-doped heterostructure.
(3) The Al(Sb,As)/AlAs quantum dots forming in the AlAs anionic sublattice demonstrate the directly opposite behavior: the smallest blue-shift occurs for the *n*-doped heterostructure and the largest one for the *p*-doped heterostructure.

4. Discussion

The material intermixing in the studied heterostructures occurs through the vacancy formation in the corresponding AlAs sublattice. Therefore, the material intermixing degree during annealing is determined by the vacancy formation rate [41]. In the next subsection, we extend our model, developed in [16] for the vacancy formation in the cationic sublattice of neutral crystals, and consider the vacancy formation dynamics in the cationic and anionic sublattices of AlAs depending on the doping level.

4.1. Vacancy Formation Dynamics

Vacancies can be formed in different mechanisms. The main paths are a generation at the surface (Schottky defect formation) and in the volume (Frenkel pair formation). In the first case, to consider the vacancy formation, it is necessary to take into account the surface structure [42–46] and the free surface exchange by atoms and molecules with the environment [28,47–49]. Frenkel pair formation is considered an unlikely source of vacancies for most semiconductor materials due to the high formation energy. However, here we focus on the processes occurring deep in the material volume only. Therefore, we neglect the defects formation and recombination at the surface (Schottky defects), as well as the defects diffusion from and to the surface. The vacancy density in our study is ruled by the temperature-activated generation of Frenkel pairs (interstitial atom and vacancy). We also do not take into account the complex defects creation, such as bi-vacancies and

vacancy-point defect complexes. In a uniform bulk crystal, the vacancy concentration (N_V) dynamics are described by the equation:

$$\frac{\partial N_V(t)}{\partial t} = G(t) - R(t), \tag{1}$$

where G is a vacancy formation rate and R is a vacancy recombination rate. The vacancy formation rate is the Arrhenius function $A \cdot \exp(-H_A/kT)$ with pre-exponential factor A, activation enthalpy H_A, and k is the Boltzmann constant. The pre-exponential factor can be written as:

$$A = \gamma_c N_{AP} N_{IP} \nu \exp\left[\frac{S_f + S_m}{k}\right], \tag{2}$$

where N_{AP} is the number of atoms that can go to an interstitial place with a vacancy formation, N_{IP} is the number of interstitial places near N_{AP} atoms (in a uniform bulk crystal $N_{AP} = N_{IP} = N$, where N is the atom density in an appropriate sublattice), ν is the Debye frequency, S_f and S_m are formation and migration entropies, and γ_c is a coefficient that depends on the interaction mechanism between a vacancy and an interstitial atom. We have shown recently that one can use $\gamma_c = a^3$, where a is a lattice constant [16]. The activation enthalpy of the vacancy formation is $H_A = H_f + H_m$, where H_f is a formation enthalpy and H_m is a migration enthalpy [26,30]. Note that, typically, the interstitial migration has lower migration barriers, compared to vacancies [50]. Therefore, we relate here H_m to the interstitial atom migration. The vacancies recombination rate can be written as:

$$R = a^3 N_V N_I \nu \exp\left[\frac{S_m}{k}\right] \exp\left[-\frac{H_m}{kT}\right], \tag{3}$$

with an interstitial atom and vacancies concentration N_I and N_V, respectively. One can write the neutral vacancy formation and recombination rates in the following manner:

$$G = N^2 G^0,\ G^0 = a^3 \nu \exp\left[\frac{S_f + S_m}{kT}\right] \exp\left[-\frac{H_f^0 + H_m^0}{kT}\right] \tag{4a}$$

$$R = N_V N_I R^0,\ R^0 = a^3 \nu \exp\left[\frac{S_m}{k}\right] \exp\left[-\frac{H_m}{kT}\right], \tag{4b}$$

where H_f^0 and H_m^0 are neutral vacancy formation and migration enthalpies, respectively.

The solution of Equation (1), taking into account Expressions (4a) and (4b), gives, in thermodynamic equilibrium, a well-known expression for the equilibrium concentration for neutral vacancies formed by the Frenkel mechanism, which does not depend on the state of the crystal electronic subsystem:

$$N_V^0 = N \exp\left[\frac{S_f}{2k}\right] \exp\left[-\frac{H_f^0}{2kT}\right]. \tag{5}$$

The generation of neutral vacancies induces a change in the atomic subsystem of a crystal only, and doping does not affect this process. Here, we will consider the charged vacancy formation dynamics in doped heterostructures. To simplify it, we will use the wide-gap crystal approximation, in which the intrinsic electron and hole concentrations are much smaller than the dopant concentration. In addition, we will assume, for simplicity, that the vacancy can be neutral or have different charge states, while the interstitial atom is neutral. The recombination of Frenkel pair occurs only when the interstitial atom is located in the nearest internode to the vacancy (short-range interaction limit).

The charged vacancy activation enthalpy is $H_A^j = H_A^0 + \Delta E_G^{V(j)}$. The index j shows the charge state of vacancy. For the negatively charged vacancy, the term $\Delta E_G^{V(-j)}$ equals $\sum_{i=1}^{j}\left(E_V^i - F\right)$, where F is the Fermi energy and E_V^i is the *-i* charged vacancy ionization energy [23,26,29], while for the positively charged vacancy $\Delta E_G^{V(+j)} = \sum_{l=1}^{j}\left(F - E_V^l\right)$, where E_V^l is the *+l* charged vacancy ionization energy as it is shown schematically in Figure 5 for single-charged vacancies. Here and below, all energies are measured relative to the top of the valence band (E_{vb}).

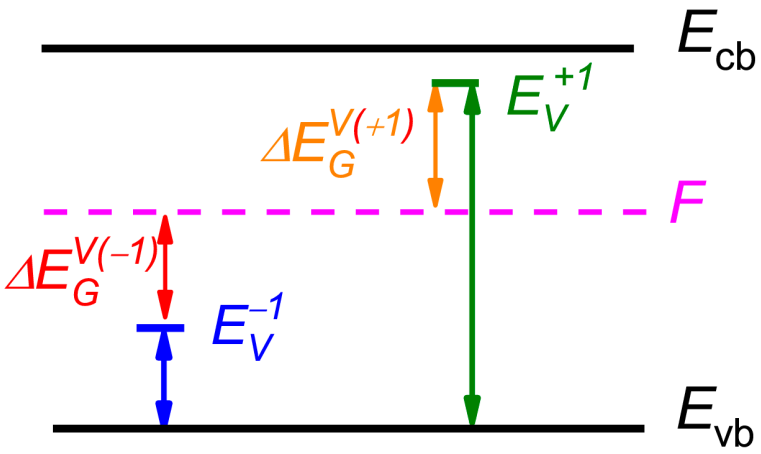


Figure 5. Band diagram for charged vacancies. Vertical arrows: olive and blue—positive and negative ionization energy of a charged vacancy, red and orange—energy gap between the vacancy ionization energy and Fermi energy (dashed magenta). Zero energy level is the valence band top.

For the negatively charged vacancy that captures j electrons at the formation, the pre-exponential factor is corrected to a probability of these electrons to be at the spatial point of the vacancy formation, since an electron's probability to be at the crystal cell, where the vacancy is created, equals the ratio of free electron concentration (n) to the conduction band density of states (N_{ce}) [51]. In a uniform bulk crystal, one has $N_{AP} = N_{IP} = N(n/N_{ce})^j$. For a positively charged vacancy that emits l electrons at generation, on the contrary, the pre-exponential factor is corrected to a probability to have a free place for the emitted electrons at the spatial point of the vacancy formation $N_{AP} = N_{IP} = N(p/N_{vh})^l$, where p is a free hole concentration and N_{vh} is a valence band density of states [51].

For the case of a non-degenerate semiconductor, when $E_{cb} - F \le kT$ ($F - E_{vb} \le kT$), where E_{cb} is the conduction band edge energy, there is a relation $n = N_{ce}\exp[(F - E_{cb})/kT]$ ($p = N_{vh}\exp[(E_{vb} - F)/kT]$). Therefore, the product of the cells number in which a $j(l)$-charged vacancy can be formed and the correspondent interstitials number is $N_{AP} \times N_{IP} = N^2(n/N_{ce})^{2j} = N^2\exp[2j(F - E_{cb})/kT]$ ($N^2(p/N_{vh})^{2l} = N^2\exp[-2lF/kT]$), and one can write the vacancy formation rate for a negatively (positively) charged vacancy as:

$$G^{-j} = a^3\nu\, N^2 \exp\left[2j\frac{F - E_{cb}}{kT}\right]\exp\left[\frac{S_f + S_m}{k}\right]\exp\left[-\frac{H_A^0 + \sum_{i=0}^{j} E_V^i - jF}{kT}\right], \quad (6a)$$

$$G^{+l} = a^3\nu\, N^2 \exp\left[-2l\frac{F}{kT}\right]\exp\left[\frac{S_f + S_m}{k}\right]\exp\left[-\frac{H_A^0 - \sum_{i=0}^{l} E_V^i + lF}{kT}\right]. \quad (6b)$$

According to Equation (6), the change in the formation probability of a vacancy with charge $j(l)$, with respect to the neutral one, is determined by the factor $\Delta_{-j} = j(2E_{cb} - 3F) + \sum_{i=1}^{j} E_V^i$ for the negatively charged vacancy and the factor $\Delta_{+l} = 3lF - \sum_{i=1}^{l} E_V^i$ for the positively charged one. Both factors are the functions of Fermi level position that depends on the carrier concentration. Under the $\Delta_{-j} > 0$ ($\Delta_{+l} > 0$) condition, the neutral vacancy formation probability will exceed that for the negatively (positively) charged ones, and vice versa for $\Delta_{-j} < 0$ ($\Delta_{+l} < 0$).

Factors Δ_{-j} and Δ_{+l}, calculated for a model material with $E_g = 1$ eV and single-charged vacancies with the ionization energies of $E_V^{-1} = 0.1$ eV and $E_V^{+1} = 0.8$ eV as the function of Fermi level position, are shown in Figure 6. The Fermi energy appropriated to $\Delta_{-1} < 0$ should be shifted into the conduction band direction and to $\Delta_{+1} < 0$ into the valence band direction.

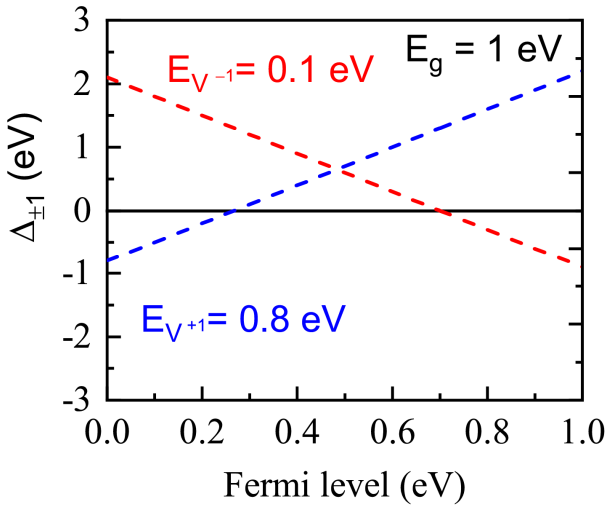


Figure 6. The Δ_{-j} (red) and $\Delta+_l$ (blue) values calculated as functions of the Fermi level position (0 corresponding to $F = E_{vb}$ and 1 to $F = E_{cb}$, respectively) for a model material with $E_g = 1$ eV and single-charged vacancies with the electron ionization energies of $E_V^{-1} = 0.1$ eV and $E_V^{+1} = 0.8$ eV.

Since various charge states are possible for a vacancy at a generation, the vacancy can be recharged after the formation. The kinetics of the neutral (N_{VC}^0) and single negatively charged (N_{VC}^{-1}) cationic vacancy concentrations, as well as neutral (N_{VA}^0) and single-positively charged (N_{VA}^{+1}) anionic vacancy concentrations, are described by the systems of kinetic equations that are presented in Appendix A.

Let us demonstrate the vacancies concentration dynamics in the bulk AlAs crystal. It is known that, for III-V compounds, the vacancy is found to exist in 0, −1, −2, and −3 charge states in the cationic sublattice and in 0, +1, +2, and +3 charge states in the anionic sublattice [52]. However, even for well-studied GaAs, the vacancy formation and migration enthalpies are still the subject of debates [24,29,53–60]. A fortiori, the vacancy formation parameters and their ionization energy in the different charged states for AlAs, are not well-established data. Therefore, one cannot quantitatively describe the vacancy formation dynamics. Here we will take into account neutral and single charged vacancies only, and that approximation is quite enough to qualitatively demonstrate the charge-carriers effect on the vacancy creation. Some vacancy parameters for AlAs (proposed in the literature) are presented in Table 1. Since the configuration entropy has a dominant contribution in S_f and S_m parameter values [28], in our estimated calculation, we used the formation and migration entropy values determined for GaAs, which is the crystal with a lattice similar to that for AlAs [55,59]. In general, vacancy migration enthalpies differ in different

sublattices. However, for simplicity, we can assume that $H_m^0(V_{Al}) \approx H_m^0(V_{As})$. We use here H_m^0 = 2.72 eV determined for AlGaAs [61]. The AlAs Debye frequency was determined, following [62], as $\nu = (TD_{AlAs}/TD_{GaAs}) \cdot \nu_{GaAs}$, where TD_{AlAs} and TD_{GaAs} are AlAs and GaAs Debye temperatures, respectively, and ν_{GaAs} is the GaAs Debye frequency [28]. The vacancy ionization levels taken from [63,64] are the same as for GaAs.

Table 1. Vacancy parameters in AlAs used in calculation: formation enthalpy H_f^0 and entropy S_f, migration enthalpy H_m^0 and entropy S_m, ionization energy in different charged states E_V^{-1} / E_V^{+1}, and ν is the AlAs Debye frequency.

Parameter	Al Vacancy Value	As Vacancy Value
H_f^0 (eV)	3.62 [24]	3.83 [24]
H_m^0 (eV)	2.72 [61]	
S_f	7.3 × k [59]	
S_m	11.3 × k [55]	
ν (Hz)	1.3×10^{13}	
E_V^{-1}/E_V^{+1} (eV)	E_{vb} + 0.11 [64]	E_{cb} − 0.14 [63]

The effect of charged vacancy creation on the Fermi energy that reflects the change in the charge-carrier concentration in a crystal was calculated with the used neutrality equation.

The calculation results are presented in Figure 7. The Fermi energy position is determined by the doping type and level. When the charged vacancy concentration exceeds the free charge carrier concentration, the Fermi energy is controlled by the concentration of charged vacancy.

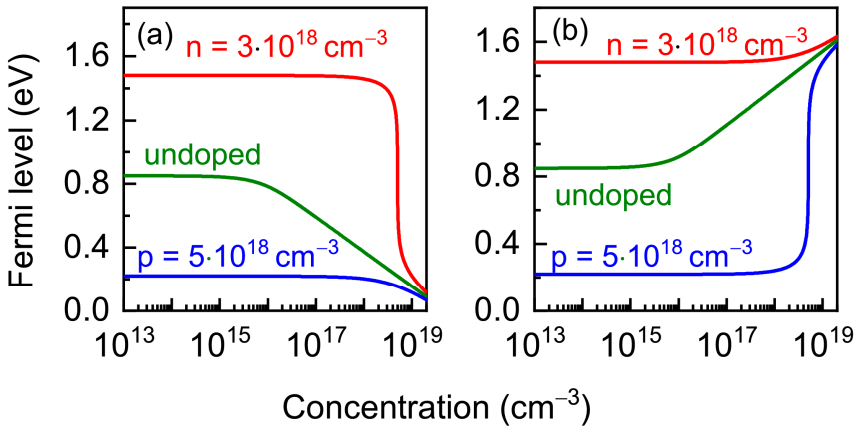


Figure 7. Fermi level energy calculated in AlAs as a function of the negatively V_{Al} (**a**) and positively V_{As} (**b**) charged vacancy concentration for temperature 1100 K (E_g = 1.822 eV). Cases: $N_A << N_D = 3 \times 10^{18}$ cm^{-2} (red), undoped (olive) and $N_D << N_A = 5 \times 10^{18}$ cm^{-2} (blue).

The dynamics of neutral and charged vacancy concentrations, as well as the ratio of charged vacancy to equilibrium neutral vacancy concentrations (N_V^{0E}), were calculated in cationic (Figure 8a,c) and anionic (Figure 8b,d) AlAs sublattices for different doping levels. The vacancy concentration rises with saturation. For cationic sublattices, the charged vacancy concentration exceeds the neutral ones in all cases. However, the saturation level for the charged V_{Al} vacancy concentration in undoped and p-doped AlAs corresponds to the equilibrium neutral vacancies concentration which shown by orange line (see Figure 8a). In undoped and p-doped cases, the factor Δ_{-1} that reflected the formation probability of charged vacancy, with respect to the neutral one, in the cationic sublattice is positive. Therefore, the vacancies appear mainly as a result of the neutral Frenkel pair formation

and those capturing electrons after the pair separation. On the other hand, in the *n*-doped material, the charged vacancy concentration V_{Al} exceeds strongly the equilibrium neutral vacancies concentration, and that corresponds to the case of negative factor Δ_{-1}.

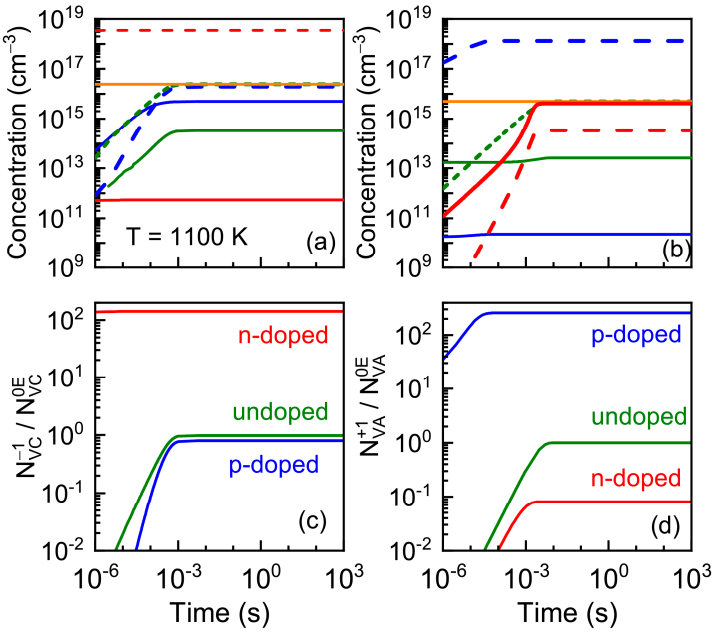


Figure 8. Dynamics of the neutral (solid lines) and single-charged (dashed lines) vacancy concentration (**a**,**b**), as well as the ratio of the charged vacancy to equilibrium neutral vacancy concentrations N_V^{0E} (**c**,**d**), calculated at different doping levels (red—*n*-doped (with donor concentration 3×10^{18} cm^{-3}), blue—*p*-doped (with acceptor concentration 5×10^{18} cm^{-3}), olive—undoped) at T = 1100 K for: (**a**,**c**) the cationic AlAs sublattice, (**b**,**d**) the anionic AlAs sublattice.

In the anionic sublattice, the charged vacancy concentration V_{As} strongly exceeds the equilibrium neutral vacancy concentration (shown by orange line) in the *p*-doped material ($\Delta_{+1} < 0$), while, in the undoped AlAs, the saturation level for the charged V_{As} vacancy concentration corresponds to the equilibrium neutral vacancies concentration, and in the case of the *n*-doped material, neutral vacancies dominate over charged ones, as it is shown in Figure 8b, and that corresponds to $\Delta_{+1} > 0$. In both of these, cases the neutral vacancy concentration does not reach the equilibrium concentration, and that indicates that charging of the vacancies is produced as a result of the neutral pair generation.

Since vacancies control interdiffusion in III–V heterostructures [65,66], the diffusivity factor for substitution impurities (D) is proportional to the vacancy concentration [41]. Therefore, we take into account that indium (antimony) diffusion $D = D_V N_V / N$ in the (In,Al)As/AlAs (Al(Sb,As)/AlAs) heterostructure can be described by the equation:

$$\frac{\partial C_{In}(z,t)}{\partial t} = \frac{D_{VC}}{N} \frac{\partial}{\partial z} \left[\left(N_{VC}^{0}(z,t) + N_{VC}^{-1}(z,t) \right) \frac{\partial}{\partial z} C_{In}(z,t) \right], \tag{7a}$$

$$\frac{\partial C_{Sb}(z,t)}{\partial t} = \frac{D_{VA}}{N} \frac{\partial}{\partial z} \left[\left(N_{VA}^{0}(z,t) + N_{VA}^{+1}(z,t) \right) \frac{\partial}{\partial z} C_{Sb}(z,t) \right]. \tag{7b}$$

The change in the generation rate and, as a consequence, the charged vacancy concentration in bulk AlAs with a change in the doping type and level (which determines the Fermi level position) provides a qualitative explanation of our experimental results (the acceleration of In diffusion in *n*-doped structures and the acceleration of Sb diffusion in *p*-doped structures). However, it is necessary to consider one more feature of heterostructures revealed in [16], which, as shown in the next subsection, can have a noticeable effect on the spatial distribution of the charged vacancy creation rate.

4.2. Spatial Distribution of Vacancy Generation Rate in Heterostructures

The fundamental difference between a bulk semiconductor and a heterostructure with QWs and QDs is the spatial distribution of electrons and holes [16]. A bulk semiconductor (except near a surface region) has a uniform equilibrium charge carrier distribution. Therefore, the spatial distribution of the charged vacancy generation rate in the bulk material is also uniform. The situation is changed drastically in heterostructures with QWs and QDs. The charge carriers are captured from the matrix in a region with a smaller bandgap, and that results in the nonuniform spatial concentration of electrons and holes in the heterostructure, as is shown in Figure 9. The nonuniform carrier distribution results in the band bending, as one can see in these figures. Therefore, the vacancy creation rate becomes spatially uneven. As has been shown recently in [16], the local generation rate of a charged vacancy changing in the region around QW is due to the band bending.

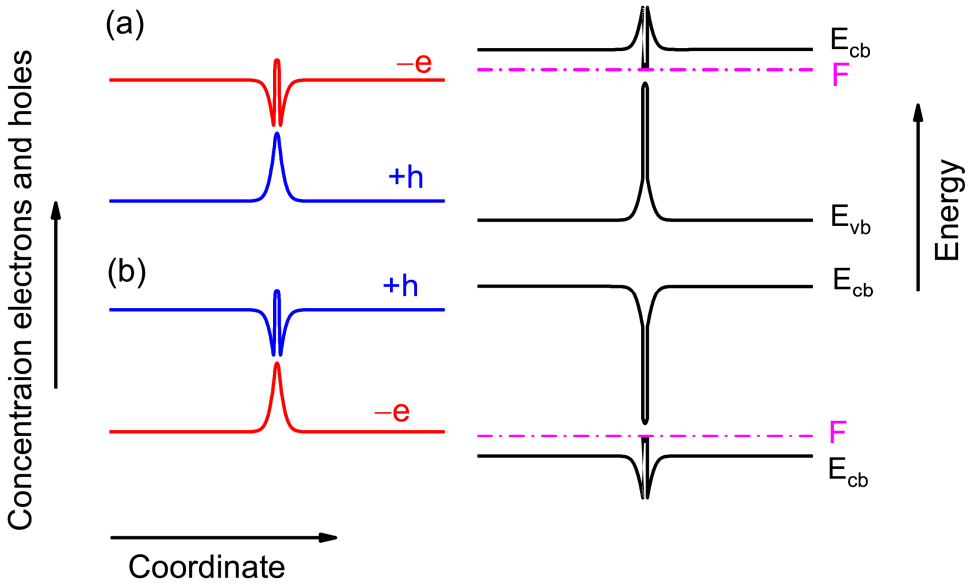


Figure 9. Schematic band diagrams and spatial electron −e and hole +h distributions. (**a**) *n*-doped heterostructure (**b**) *p*-doped heterostructure.

The dynamics of the neutral and single negatively (positively) charged vacancy concentration in the heterostructure is described by the equation systems that are presented in Appendix B.

4.3. Band Diagrams of Heterostructures with QDs and Carrier Distribution

Let us look at the energy diagram calculated at high temperatures for (In,Al)As/AlAs and Al(Sb,As)/AlAs heterostructures with QDs in order to demonstrate the spatially uneven charge-carrier distribution. The energy spectra of heterostructures and charge distribution were calculated using the NEXTNANO3 nanodevice simulation tool [67]. Lattice constants, effective masses of electrons and holes in AlAs, InAlAs, and AlSbAs alloys, valence band offset, and its temperature dependences were taken from [68]. The calculations took into account the deformation, deformation potentials, and generation and distribution of charge carriers. The calculation methods are shown in [34,69–71]. For simplicity, the exciton correction for the energy levels was neglected.

The energy diagrams and charge-carrier distribution calculated for *n*-doped, undoped, and *p*-doped (In,Al)As/AlAs and Al(Sb,As)/AlAs heterostructures are shown in Figures 10 and 11, respectively. A specific feature of both heterostructures is that the localizing potential for electrons in the conduction band is noticeably smaller than that for holes in the valence band.

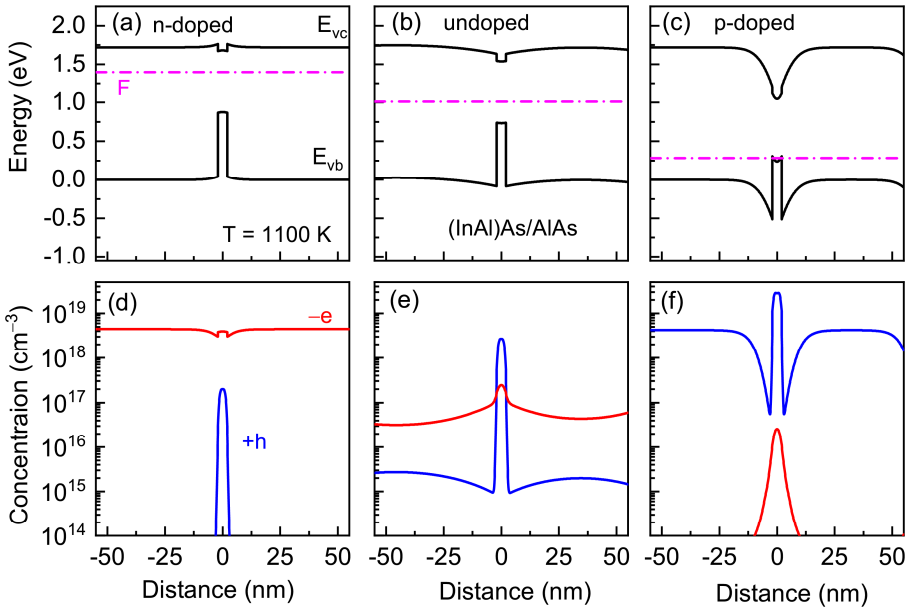


Figure 10. Band diagrams (**a**–**c**) and spatial electron −e (red) and hole +h (blue) distributions (**d**–**f**) calculated for *n*-doped (**a**,**d**), undoped (**b**,**e**), and *p*-doped (**c**,**f**) heterostructures with (In,Al)As/AlAs QDs.

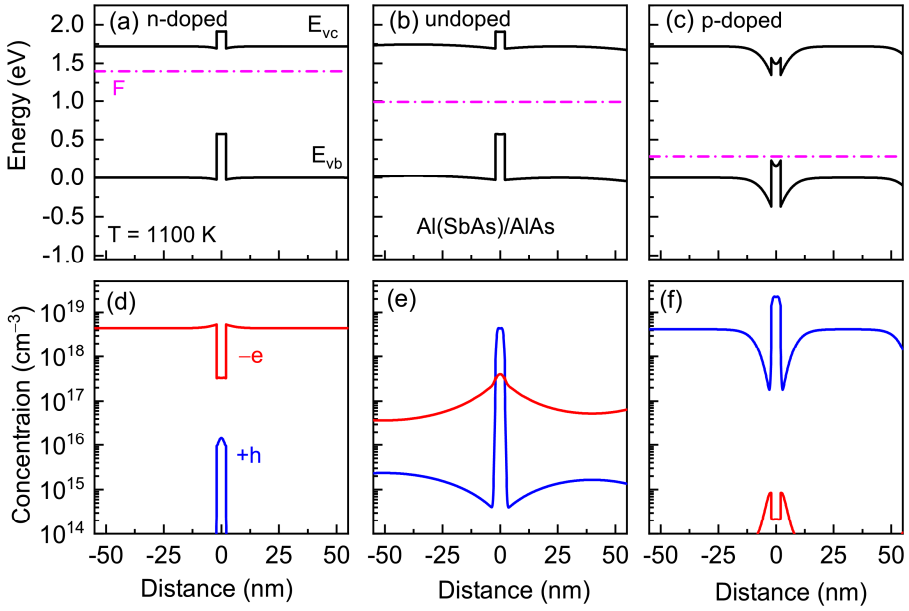


Figure 11. Band diagrams (**a**–**c**) and spatial electron −e (red) and hole +h (blue) distributions (**d**–**f**) calculated for *n*-doped (**a**,**d**), undoped (**b**,**e**), and *p*-doped (**c**,**f**) heterostructures with Al(Sb,As)/GaAs QDs.

The low electron capacity in the QD region leads to the spatial electron distribution in *n*-doped heterostructures, which is very similar to that in bulk AlAs. As a result, in the *n*-doped heterostructures with (In,Al)As/AlAs QDs, the indium diffusivity factor, that is determined by the negatively charged Al vacancy distribution, is practically spatially uniform as in a bulk AlAs crystal (only a small dispersion is observed near the QD/matrix interface due to a small band-bending, as it is shown in Figure 12a). However, in the p-doped heterostructures, the charge distribution is quite different from that in the n-doped ones. The collection of positively charged holes in QDs leads to a strong spatially nonuniform charge distribution. As a result, the antimony diffusivity factor, that is determined in

p-doped heterostructures with Al(Sb,As)/AlAs QDs by the positively charged As vacancy distribution, becomes spatially nonuniform (it strongly decreases near the QD/matrix interface, as is shown in Figure 12b). Note that the charge distribution in *p*-doped (*n*-doped) heterostructures does not affect the vacancy concentration and diffusivity factor distributions in (In,Al)As/AlAs QDs (Al(Sb,As)/AlAs QDs) since the neutral vacancies with the spatially uniform distribution are dominant.

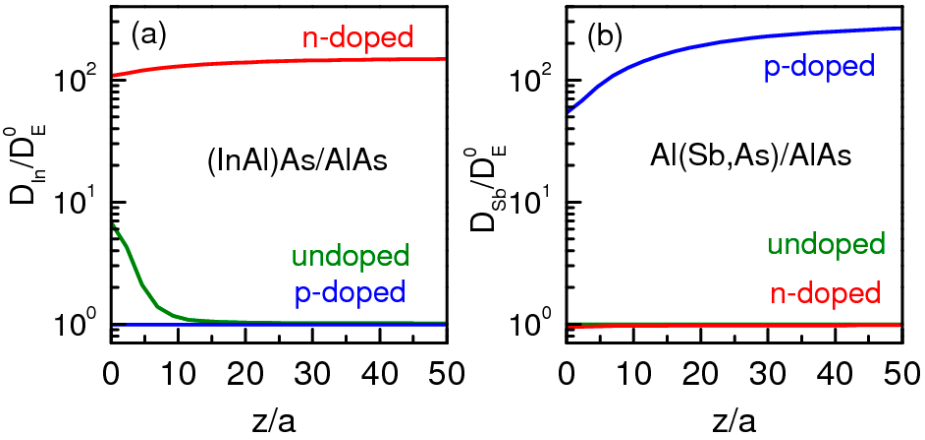


Figure 12. Diffusivity factor distribution calculated for (**a**) indium in (In,Al)As/AlAs and (**b**) antimony in Al(Sb,As)/AlAs heterostructures: *n*-doped (red), undoped (olive), and *p*-doped (blue). The diffusivity factors are normalized to the value D_E^0 determined for the neutral vacancies' equilibrium concentration.

The concentration of electrons and holes integrated over all layers in undoped heterostructures coincides due to the electrical neutrality condition. However, one can see an unbalance of electrons and holes in the QD region (see Figures 10e and 11e) arising, as we have shown recently in [16], as a result of the difference in the charge carrier generation rate in the wide-gap matrix and narrow-gap quantum dot material and a subsequent redistribution of these carriers in the heterostructure.

In the framework of our simple model, we calculated the diffusivity factor spatial distributions for p-doped (with acceptor concentration 5×10^{18} cm^{-3}), undoped, and n-doped (with donor concentration 3×10^{18} cm^{-3}) heterostructures with (In,Al)As/AlAs and Al(Sb,As)/AlAs QDs, taking into account the spatial electron and hole distributions. The calculated results are shown in Figure 12. The calculated diffusivity factors are normalized to the spatially uniformed diffusivity factor values determined for the neutral vacancies' equilibrium concentration. One can see that increasing the electron density in the QD/matrix heterojunction region increases the charged vacancy generation rate and, as a result, the indium diffusivity factor in the (In,Al)As/AlAs heterostructure. Therefore, a noticeable mixing of materials takes place even in the undoped heterostructure, as can be seen from the PL band blue-shift in Figure 4a. On the other hand, decreasing the hole density in the QD/matrix heterojunction region in the Al(Sb,As)/AlAs heterostructure results in the domination for the neutral vacancy formation that does not increase the antimony diffusivity factor. Therefore, the mixing of materials is practically the same for undoped and n-doped heterostructures, as can be seen in Figure 4b; in both cases, the PL band blue-shift is negligible. Thus, one can see that the calculations in the framework of the model give a good explanation for all features of our experimental data.

Note that, including the dynamics of complex defects (such as bi-vacancies or vacancy-point defect complexes), formation in the model will lead to insignificant quantitative changes in the calculated diffusion parameters for low vacancy concentrations. In this case, there will be a slight decrease in the diffusion coefficient, since some vacancies are excluded from the diffusion process. On the other hand, the formation of complex defects slightly affects the processes associated with the nonuniform spatial distribution of charge-carriers.

However, at high vacancy concentrations, complex defect formation can greatly change the diffusion pattern.

5. Conclusions

The effect of the charge carrier concentration on the high temperature vacancy-mediated intermixing in AlAs-based heterostructures with QDs formed in the cationic and anionic sublattices was studied. The intermixing degree in the cationic (anionic) sublattice is accelerated with the increases in the electron (hole) concentration as a result of an increase in the negatively (positively) charged vacancy formation rate. We demonstrated that the diffusion coefficient in such heterostructures can be nonuniform, and that is due to the nonuniformity for the charged vacancy creation that stems from a gradient of the carrier concentration in the QD/matrix heterointerface region. Space charge regions arise in the heterostructures due to the carriers capture in the QDs from the doped matrix. A theoretical model of the vacancy-mediated high-temperature diffusion in doped semiconductor heterostructures was developed. The features of experimental data are well explained in the framework of this model.

Author Contributions: Conceptualization, methodology, theoretical investigation, T.S.S.; data collection, V.V.A.; writing—original draft preparation, T.S.S. and V.V.A.; writing—review and editing, T.S.S. and V.V.A.; visualization, T.S.S.; project administration, T.S.S.; funding acquisition, T.S.S. All authors have read and agreed to the published version of the manuscript.

Funding: This work was supported by the Russian Science Foundation (grant no. 22-12-00022).

Institutional Review Board Statement: Not applicable.

Informed Consent Statement: Not applicable.

Data Availability Statement: Data are available from the authors on request.

Conflicts of Interest: The authors declare no conflict of interest.

Appendix A

The kinetics of the neutral (N_{VC}^0) and single negatively charged (N_{VC}^{-1}) vacancy concentration in the cationic sublattice is described by the system of kinetic equations:

$$\begin{array}{l} N_{IC}(t) = N_{VC}^0(t) + N_{VC}^{-1}(t), \\ N_{ce}\exp\left[\frac{F(t)-E_{cb}}{kT}\right] - N_{vh}\exp\left[-\frac{F(t)}{kT}\right] + N_{VC}^{-1}(t) - N_D + N_A = 0, \end{array} \quad \text{(A1)}$$

where G_C^0 and R_C^0 are neutral vacancy creation and recombination probabilities in the cationic sublattice, and γ^- is a trapping coefficient of an electron for a neutral vacancy. N_D and N_A are shallow donor and acceptor concentrations (at high temperatures, all impurities are assumed to be ionized). Note that, here and in what follows, we examine a low compensated semiconductor with $N_A << N_D$ or $N_D << N_A$.

In the case of the neutral (N_{VA}^0) and single positively charged (N_{VA}^{+1}) vacancies in the anionic sublattice, the system of kinetic equations is:

$$\begin{array}{l} \frac{\partial N_{VA}^0(t)}{\partial t} = N^2 G_A^0 - N_{VA}^0(t) N_{IA}(t) R_A^0 - \gamma^+ N_{VA}^0(t) + \gamma^+ N_{VA}^{+1}(t)\exp\left[-\frac{E_V^{+1}-F(t)}{kT}\right], \\ \frac{\partial N_{VA}^{+1}(t)}{\partial t} = N^2 G_{\mathrm{A}}^0 \exp\left[\frac{E_V^{+1}-3F(t)}{kT}\right] - N_{VA}^{+1}(t) N_{IA}(t) R_A^0 + \gamma^+ N_{VA}^0(t) - \gamma^+ N_{VA}^{+}(t)\exp\left[-\frac{E_V^{+1}-F(t)}{kT}\right], \\ N_{IA}(t) = N_{VA}^0(t) + N_{VA}^{+1}(t), \\ N_{ec}\exp\left[\frac{F(t)-E_{cb}}{kT}\right] - N_{vh}\exp\left[-\frac{F(t)}{kT}\right] - N_{VA}^{+1}(t) - N_D + N_A = 0 \end{array} \quad \text{(A2)}$$

where G_A^0 and R_A^0 are neutral vacancy generation and recombination probability in the anionic sublattice, and γ^+ is a coefficient of an electron emission from a neutral vacancy.

Appendix B

The dynamics of the neutral and single negatively charged vacancy concentrations in the heterostructure can be described as:

$$\begin{aligned}
&\frac{\partial N^0_{VC}(z,t)}{\partial t} = N^2 G^0_C - N^0_{VC}(z,t) N_{IC}(z,t) R^0_C - \gamma^- N^0_{VC}(z,t) + \gamma^- N^{-1}_{VC}(z,t) \exp\left[\frac{F(t)-E^{-1}_V(z,t)}{kT}\right] + D_{VC}\left[\frac{\partial^2 N^0_{VC}(z,t)}{\partial z^2}\right],\\
&\frac{\partial N^{-1}_{VC}(z,t)}{\partial t} = N^2 G^0_C \exp\left[-\frac{E^{-1}_V(z,t)+2E_{cb}(z,t)-3F(t)}{kT}\right] + \gamma^- N^0_{VC}(z,t) -\\
&\gamma^- N^{-1}_{VC}(z,t) \exp\left[-\frac{F(t)-E^{-1}_V(z,t)}{kT}\right] - N^{-1}_{VC}(z,t) N_{IC}(t) R^0_C + D_V\left[\frac{\partial^2 N^{-1}_{VC}(z,t)}{\partial z^2}\right],\\
&N_{ec} \exp\left[\frac{F(t)-E_{cb}(z,t)}{kT}\right] - N_{vh} \exp\left[-\frac{F(t)}{kT}\right] + N^{-1}_{VC}(z,t) - N_D + N_A = 0,\\
&\frac{\partial C_{In}(z,t)}{\partial t} = \frac{D_{VC}}{N}\frac{\partial}{\partial z}\left[\left(N^0_{VC}(z,t) + N^{-1}_{VC}(z,t)\right)\frac{\partial}{\partial z} C_{In}(z,t)\right],
\end{aligned} \tag{A3}$$

and, for the case of neutral and single positively charged vacancies, as:

$$\begin{aligned}
&\frac{\partial N^0_{VA}(z,t)}{\partial t} = N^2 G^0_A - N^0_{VA}(z,t) N_{IC}(z,t) R^0_A + \gamma^+ N^{+1}_{VA}(z,t) - \gamma^+ N^0_{VA}(z,t) \exp\left[\frac{F(t)-E^{+1}_V(z,t)}{kT}\right] + D_{VA}\left[\frac{\partial^2 N^0_{VA}(z,t)}{\partial z^2}\right],\\
&\frac{\partial N^{+1}_{VA}(z,t)}{\partial t} = N^2 G^0_A \exp\left[-\frac{3F(t)-E^{+1}_V(z,t)}{kT}\right] - \gamma^+ N^{+1}_{VA}(z,t) + \gamma^+ N^0_{VC}(z,t) \exp\left[\frac{F(t)-E^{+1}_V(z,t)}{kT}\right] -\\
&N^{+1}_{VA}(z,t) N_{IA}(t) R^0_A + D_{VA}\left[\frac{\partial^2 N^{+1}_{VA}(z,t)}{\partial z^2}\right],\\
&N_{ec} \exp\left[\frac{F(t)-E_{cb}(z,t)}{kT}\right] - N_{vh} \exp\left[-\frac{F(t)}{kT}\right] - N^{+1}_{VA}(z,t) - N_D + N_A = 0,\\
&\frac{\partial C_{Sb}(z,t)}{\partial t} = \frac{D_{VA}}{N}\frac{\partial}{\partial z}\left[\left(N^0_{VA}(z,t) + N^{+1}_{VA}(z,t)\right)\frac{\partial}{\partial z} C_{Sb}(z,t)\right].
\end{aligned} \tag{A4}$$

References

1. Kalt, H.; Hetterich, M. (Eds.) *Optics of Semiconductors and Their Nanostructures*; Springer: Berlin, Germany, 2004.
2. Ivchenko, E.L.; Pikus, G.E. *Superlattices and Other Heterostructures*; Springer Series in Solid-State Sciences; Springer: Berlin, Germany, 1997; Volume 110.
3. Abramkin, D.S.; Atuchin, V.V. Novel InGaSb/AlP Quantum Dots for Non-Volatile Memories. *Nanomaterials* **2022**, *12*, 3794. [CrossRef]
4. Smirnov, D.S.; Shamirzaev, T.S.; Yakovlev, D.R.; Bayer, M. Dynamic Polarization of Electron Spins Interacting with Nuclei in Semiconductor Nanostructures. *Phys. Rev. Lett.* **2020**, *125*, 156801. [CrossRef]
5. Shamirzaev, T.S.; Shumilin, A.V.; Smirnov, D.S.; Rautert, J.; Yakovlev, D.R.; Bayer, M. Dynamic polarization of electron spins in indirect band gap (In,Al)As/AlAs quantum dots in a weak magnetic field: Experiment and theory. *Phys. Rev. B* **2021**, *104*, 115405. [CrossRef]
6. Abramkin, D.S.; Petrushkov, M.O.; Bogomolov, D.B.; Emelyanov, E.A.; Yesin, M.Y.; Vasev, A.V.; Bloshkin, A.A.; Koptev, E.S.; Putyato, M.A.; Atuchin, V.V.; et al. Structural Properties and Energy Spectrum of Novel GaSb/AlP Self-Assembled Quantum Dots. *Nanomaterials* **2023**, *13*, 910. [CrossRef]
7. Zhou, Y.; Luo, X.; Yang, J.; Qiu, Q.; Xie, T.; Liang, T. Application of Quantum Dot Interface Modification Layer in Perovskite Solar Cells: Progress and Perspectives. *Nanomaterials* **2022**, *12*, 2102. [CrossRef] [PubMed]
8. Smponias, A.; Stefanatos, D.; Paspalakis, E. Efficient Biexciton Preparation in a Quantum Dot—Metal Nanoparticle System Using On-Off Pulses. *Nanomaterials* **2021**, *11*, 1859. [CrossRef]
9. Petrushkov, M.O.; Abramkin, D.S.; Emelyanov, E.A.; Putyato, M.A.; Komkov, O.S.; Firsov, D.D.; Vasev, A.V.; Yesin, M.Y.; Bakarov, A.K.; Loshkarev, I.D.; et al. Dislocation Filter Based on LT-GaAs Layers for Monolithic GaAs/Si Integration. *Nanomaterials* **2022**, *12*, 4449. [CrossRef] [PubMed]
10. Kuznetsova, M.S.; Rautert, J.; Kavokin, K.V.; Smirnov, D.S.; Yakovlev, D.R.; Bakarov, A.K.; Gutakovskii, A.K.; Shamirzaev, T.S.; Bayer, M. Electron-nuclei interaction in the X valley of (In,Al)As/AlAs quantum dots. *Phys. Rev. B* **2020**, *101*, 075412. [CrossRef]
11. Shamirzaev, T.S.; Rautert, J.; Yakovlev, D.R.; Debus, J.; Gornov, A.Y.; Glazov, M.M.; Ivchenko, E.L.; Bayer, M. Spin dynamics and magnetic field induced polarization of excitons in ultrathin GaAs/AlAs quantum wells with indirect band gap and type-II band alignment. *Phys. Rev. B* **2017**, *96*, 035302. [CrossRef]
12. Taylor, M.W.; Spencer, P.; Murray, R. Negative circular polarization as a universal property of quantum dots. *Appl. Phys. Lett.* **2015**, *106*, 122404. [CrossRef]
13. Debus, J.; Shamirzaev, T.S.; Dunker, D.; Sapega, V.F.; Ivchenko, E.L.; Yakovlev, D.R.; Toropov, A.I.; Bayer, M. Spin-flip Raman scattering of the Γ-X mixed exciton in indirect band gap (In,Al)As/AlAs quantum dots. *Phys. Rev. B* **2014**, *90*, 125431. [CrossRef]
14. Li, E.H. *Semiconductor Quantum Wells Intermixing*; Gordon and Breach: Amsterdam, The Netherlands, 2000.
15. Gupta, D. (Ed.) *Diffusion Processes in Advanced Technological Materials*; Springer: New York, NY, USA, 2005.

16. Shamirzaev, T.S.; Atuchin, V.V.; Zhilitskiy, V.E.; Gornov, A.Y. Dynamics of Vacancy Formation and Distribution in Semiconductor Heterostructures: Effect of Thermally Generated Intrinsic Electrons. *Nanomaterials* **2023**, *13*, 308. [CrossRef]
17. Shamirzaev, T.S.; Debus, J.; Abramkin, D.S.; Dunker, D.; Yakovlev, D.R.; Dmitriev, D.V.; Gutakovskii, A.K.; Braginsky, L.S.; Zhuravlev, K.S.; Bayer, M. Exciton recombination dynamics in an ensemble of (In,Al)As/AlAs quantum dots with indirect band-gap and type-I band alignment. *Phys. Rev. B* **2011**, *84*, 155318. [CrossRef]
18. Sinha, S.S.K.; Kumar, S.; Das, M.K. Dot size variability induced changes in the optical absorption spectra of interdiffused quantum dot systems. *Appl. Phys. A* **2019**, *125*, 774. [CrossRef]
19. Petrov, M.Y.; Ignatiev, I.; Poltavtsev, S.; Greilich, A.; Bauschulte, A.; Yakovlev, D.; Bayer, M. Effect of thermal annealing on the hyperfine interaction in InAs/GaAs quantum dots. *Phys. Rev. B* **2008**, *78*, 045315. [CrossRef]
20. Ivanov, V.Y.; Shamirzaev, T.S.; Yakovlev, D.R.; Gutakovskii, A.K.; Owczarczyk, Ł.; Bayer, M. Optically detected magnetic resonance of photoexcited electrons in (In,Al)As/AlAs quantum dots with indirect band gap and type-I band alignment. *Phys. Rev. B* **2018**, *97*, 245306. [CrossRef]
21. Tartakovskii, A.I.; Makhonin, M.N.; Sellers, I.R.; Cahill, J.; Andreev, A.D.; Whittaker, D.M.; Wells, J.-P.R.; Fox, A.M.; Mowbray, D.J.; Skolnick, M.S.; et al. Effect of thermal annealing and strain engineering on the fine structure of quantum dot excitons. *Phys. Rev. B* **2004**, *70*, 193303. [CrossRef]
22. Shamirzaev, T.S.; Kalagin, A.K.; Toropov, A.I.; Gutakovskii, A.K.; Zhuravlev, K.S. Narrowing of ground energy level distribution in an array of InAs/AlAs QDs by post grown annealing. *Phys. Status Solidi C* **2006**, *3*, 3932–3934. [CrossRef]
23. Seebauer, E.G.; Kratzer, M.C. Charged point defects in semiconductors. *Mater. Sci. Eng. R Rep.* **2006**, *55*, 57–149. [CrossRef]
24. Tahini, H.A.; Chroneos, A.; Murphy, S.; Schwingenschlogl, U.; Grimes, R.W. Vacancies and defect levels in III–V semiconductors. *J. Appl. Phys.* **2013**, *114*, 063517. [CrossRef]
25. Walukiewicz, W. Amphoteric native defects in semiconductors. *Appl. Phys. Lett.* **1989**, *54*, 2094–2096. [CrossRef]
26. Zhang, S.B.; Northrup, J.E. Chemical potential dependence of defect formation energies in GaAs: Application to Ga self-diffusion. *Phys. Rev. Lett.* **1991**, *67*, 2339–2342. [CrossRef] [PubMed]
27. Vinetskii, V.L.; Kholodar, G.A. *The Statistical Interaction of Electrons and Defects in Semiconductors*; NaukovaDumka: Kiev, Ukraine, 1969. (In Russian)
28. Freysoldt, C.; Grabowski, B.; Hickel, T.; Neugebauer, J.; Kresse, G.; Janotti, A.; Van de Walle, C.G. First-principles calculations for point defects in solids. *Rev. Mod. Phys.* **2014**, *86*, 253–305. [CrossRef]
29. Baraff, G.A.; Schliiter, M. Electronic Structure, Total Energies, and Abundances of the Elementary Point Defects in GaAs. *Phys.Rev. Lett.* **1985**, *55*, 1327. [CrossRef]
30. Crawford, J.H., Jr.; Slifkin, L.M. (Eds.) Point defects in solids. In *Semiconductors and Molecular Crystals*; Plenum Press: New York, NY, USA, 1975; Volume 2.
31. Drabold, D.A.; Estreicher, S.K. (Eds.) *Theory of Defects in Semiconductors*; Springer: Berlin/Heidelberg, Germany, 2007.
32. Shamirzaev, T.S.; Nenashev, A.V.; Gutakovskii, A.K.; Kalagin, A.K.; Zhuravlev, K.S.; Larsson, M.; Holtz, P.O. Atomicandenergystructureof InAs/AlAsquantumdots. *Phys. Rev. B* **2008**, *78*, 085323. [CrossRef]
33. Abramkin, D.S.; Rumynin, K.M.; Bakarov, A.K.; Kolotovkina, D.A.; Gutakovskii, A.K.; Shamirzaev, T.S. Quantum dotsformed in InSb/AlAsandAlSb/AlAsheterostructures. *JETP Lett.* **2016**, *103*, 692. [CrossRef]
34. Shamirzaev, T.S.; Yakovlev, D.R.; Kopteva, N.E.; Kudlacik, D.; Glazov, M.M.; Krechetov, A.G.; Gutakovskii, A.K.; Bayer, M. Spin dynamics of charged excitons in ultrathin (In,Al)(Sb,As)/AlAs and Al(Sb,As)/AlAs quantum wells with an indirect band gap. *Phys. Rev. B* **2022**, *106*, 075407. [CrossRef]
35. Shamirzaev, T.S.; Yakovlev, D.R.; Bakarov, A.K.; Kopteva, N.E.; Kudlacik, D.; Gutakovskii, A.K.; Bayer, M. Recombinationandspin-dynamicsofexcitons in thin (Ga,Al)(Sb,As)/AlAsquantumwellswith an indirect band gapand type-I band alignment. *Phys. Rev. B* **2020**, *102*, 165423. [CrossRef]
36. Shamirzaev, T.S.; Abramkin, D.S.; Dmitriev, D.V.; Gutakovskii, A.K. Nonradiative energy transfer between vertically coupled indirect and direct bandgap InAs quantum dots. *Appl. Phys. Lett.* **2010**, *97*, 263102. [CrossRef]
37. Shamirzaev, T.S.; Gilinsky, A.M.; Kalagin, A.K.; Toropov, A.I.; Gutakovskii, A.K.; Zhuravlev, K.S. Strong sensitivity of photoluminescence of InAs/AlAs quantum dots to defects: Evidence for lateral inter-dot transport, Semicond. *Sci. Technol.* **2006**, *21*, 527. [CrossRef]
38. Rautert, J.; Shamirzaev, T.S.; Nekrasov, S.V.; Yakovlev, D.R.; Klenovský, P.; Kusrayev, Y.G.; Bayer, M. Optical orientation and alignment of excitons in direct and indirect band gap (In,Al)As/AlAs quantum dots with type-I band alignment. *Phys. Rev. B* **2019**, *99*, 195411. [CrossRef]
39. Shamirzaev, T.S.; Shumilin, A.V.; Smirnov, D.S.; Kudlacik, D.; Nekrasov, S.V.; Kusrayev, Y.G.; Yakovlev, D.R.; Bayer, M. Optical Orientation of Excitons in a Longitudinal Magnetic Field in Indirect Band Gap (In, Al)As/AlAs Quantum Dots with Type-I Band Alignment. *Nanomaterials* **2023**, *13*, 729. [CrossRef]
40. Shamirzaev, T.S.; Nenashev, A.V.; Zhuravlev, K.S. Coexistence of direct and indirect band structures in arrays of InAs/AlAs quantum dots. *Appl. Phys. Lett.* **2008**, *92*, 213101. [CrossRef]
41. Khreis, O.M.; Gillin, W.P.; Homewood, K.P. Interdiffusion: A probe of vacancy diffusion in III-V materials. *Phys. Rev. B* **1997**, *55*, 15813–15818. [CrossRef]
42. Djie, H.S.; Gunawan, O.; Wang, D.-N.; Ooi, B.S.; Hwang, J.C.M. Group-III vacancy induced InxGa1 − xAs quantum dot interdiffusion. *Phys. Rev. B* **2006**, *73*, 155324. [CrossRef]

43. Wang, Y.; Djie, H.S.; Ooi, B.S. Group-III intermixing in InAs/InGaAlAs quantum dots-in-well. *Appl. Phys. Lett.* **2006**, *88*, 111110. [CrossRef]
44. Alahmadi, Y.; Li Kam Wa, P. Effects of selective area intermixing on InAlGaAs multiple quantum well laser diode. *Semicond. Sci. Technol.* **2019**, *34*, 025010. [CrossRef]
45. Lever, P.; Tan, H.H.; Jagadish, C. Impurity free vacancy disordering of InGaAs quantum dots. *J. Appl. Phys.* **2004**, *96*, 7544–7548. [CrossRef]
46. McKerracher, I.; Fu, L.; Tan, H.H.; Jagadish, C. Intermixing of InGaAs/GaAs quantum wells and quantum dots using sputter-deposited silicon oxynitride capping layers. *J. Appl. Phys.* **2012**, *112*, 113511. [CrossRef]
47. Rouviere, J.-L.; Kim, Y.; Cunningham, J.; Rentschler, J.A.; Bourret, A.; Ourmazd, A. Measuring properties of point defects by electron microscopy: The Ga vacancy in GaAs. *Phys. Rev. Lett.* **1992**, *68*, 2798–2801. [CrossRef] [PubMed]
48. Hurle, D.T.J. A comprehensive thermodynamic analysis of native point defect and dopant solubilities in gallium arsenide. *J. Appl. Phys.* **1999**, *85*, 6957–7022. [CrossRef]
49. Shamirzaev, T.S.; Sokolov, A.L.; Zhuravlev, K.S.; Kobitski, A.Y.; Wagner, H.P.; Zahn, D.R. Changes in the density of nonradiative recombination centers in GaAs/AlGaAs quantum-well structures as a result of treatment in CF_4 plasma. *Semiconductors* **2002**, *36*, 81–84. [CrossRef]
50. Wright, A.F.; Modine, N.A. Migration processes of the As interstitial in GaAs. *J. Appl. Phys.* **2016**, *120*, 215705. [CrossRef]
51. Grundmann, M. *The Physics of Semiconductors*; Springer: Berlin/Heidelberg, Germany, 2006.
52. Puska, M.J. Electronic structures of point defects in III-V compound semiconductors. *J. Phys. Condens. Matter* **1989**, *1*, 7347–7366. [CrossRef]
53. El-Mellouhi, F.; Mousseau, N. Self-vacancies in gallium arsenide: An ab initio calculation. *Phys. Rev. B* **2005**, *71*, 125207. [CrossRef]
54. Gebauer, J.; Lausmann, M.; Redmann, F.; Krause-Rehberg, R.; Leipner, H.S.; Weber, E.R.; Ebert, P. Determination of the Gibbs free energy of formation of Ga vacancies in GaAs by positron annihilation. *Phys. Rev. B* **2003**, *67*, 235207. [CrossRef]
55. Mitev, P.; Seshadri, S.; Guido, L.J.; Schaafsma, D.T.; Christensen, D.H. Cation vacancy formation and migration in the AlGaAsheterostructure system. *Appl. Phys. Lett.* **1998**, *73*, 3718–3720. [CrossRef]
56. Lahiri, I.; Nolte, D.D.; Melloch, M.R.; Woodall, J.M.; Walukiewicz, W. Enhanced diffusion in nonstoichiometric quantum wells and the decay of supersaturated vacancy concentrations. *Appl. Phys. Lett.* **1996**, *69*, 239–241. [CrossRef]
57. Bert, N.A.; Chaldyshev, V.V.; Musikhin, Y.G.; Suvorova, A.A.; Preobrazhenskii, V.V.; Putyato, M.A.; Semyagin, B.R.; Werner, P. In–Ga intermixing in low-temperature grown GaAs delta doped with In. *Appl. Phys. Lett.* **1999**, *74*, 1442–1444. [CrossRef]
58. Van Vechten, J.A. *Handbook on Semiconductors*; Moss, T.S., Ed.; North-Holland: Amsterdam, The Netherlands, 1980; Chapter 1; Volume 3.
59. Bockstedte, M.; Schefer, M. Theory of Self-Diffusion in GaAs. *Z. Phys. Chem.* **1997**, *200*, 195. [CrossRef]
60. Jia, Y.Q.; Bardeleben, H.J.V.; Stienvard, D.; Delerue, C. Electron-paramagnetic-resonance observation of gallium vacancy in electron-irradiated p-type GaAs. *Phys. Rev. B* **1992**, *45*, 1645. [CrossRef] [PubMed]
61. Kahen, K.B.; Peterson, D.L.; Rajeswaran, G.; Lawrence, D.J. Properties of Ga vacancies in AlGaAs materials. *Appl. Phys. Lett.* **1989**, *55*, 651. [CrossRef]
62. Ullrich, B.; Bhowmick, M.; Xi, H. Relation between Debye temperature and energy band gap of semiconductors. *AIP Adv.* **2017**, *7*, 045109. [CrossRef]
63. Saarinen, K.; Hautojärvi, P.; Lanki, P.; Corbel, C. Ionization levels of As vacancies in as-grown GaAs studied by positron-lifetime spectroscopy. *Phys. Rev. B* **1991**, *44*, 10585–10600. [CrossRef] [PubMed]
64. Pöykkö, S.; Puska, M.J.; Nieminen, R.M. *Abinitio* study of fully relaxed divacancies in GaAs. *Phys. Rev. B* **1996**, *53*, 3813. [CrossRef]
65. Marsh, J.H. Quantum well intermixing. *Semicond. Sci. Technol.* **1993**, *8*, 1136. [CrossRef]
66. Tuck, B. Mechanisms of atomic diffusion in the III-V semiconductors. *J. Phys. D Appl. Phys.* **1985**, *18*, 557–584. [CrossRef]
67. Zibold, T. Semiconductor Based Quantum Information Devices: Theory and Simulations. Ph.D. Thesis, Technische Universitat München, Munich, Germany, 2007.
68. Vurgaftman, I.; Meyer, J.R.; Ram-Mohan, L.R. Band parameters for III–V compound semiconductors and their alloys. *J. Appl. Phys.* **2001**, *89*, 5815–5875. [CrossRef]
69. Shamirzaev, T.S. Type-I semiconductor heterostructures with an indirect-gap conduction band. *Semiconductors* **2011**, *45*, 96–102. [CrossRef]
70. Abramkin, D.S.; Shamirzaev, T.S. Type-I indirect-gap semiconductor heterostructures on (110) substrates. *Semiconductors* **2019**, *53*, 703–710. [CrossRef]
71. Shamirzaev, T.S.; Gilinsky, A.M.; Kalagin, A.K.; Nenashev, A.V.; Zhuravlev, K.S. Energy spectrum and structure of thin pseudomorphicInAs quantum wells in an AlAs matrix: Photoluminescence spectra and band-structure calculations. *Phys. Rev. B* **2007**, *76*, 155309. [CrossRef]

Disclaimer/Publisher's Note: The statements, opinions and data contained in all publications are solely those of the individual author(s) and contributor(s) and not of MDPI and/or the editor(s). MDPI and/or the editor(s) disclaim responsibility for any injury to people or property resulting from any ideas, methods, instructions or products referred to in the content.